Extreme Mechanics Letters 61 (2023) 101997

Contents lists available at ScienceDirect

Extreme Mechanics Letters

journal homepage: www.elsevier.com/locate/eml

Flexoelectricity at fractal rough surfaces

Chongpu Zhai [a], Shuwen Zhang [a], Hui Ji [a], Deheng Wei [b], Hengxu Song [c,d], Kaiyuan Liu [a,e,*], Minglong Xu [a,**]

[a] State Key Laboratory for Strength and Vibration of Mechanical Structures, School of Aerospace Engineering, Xi'an Jiaotong University, Xi'an, 710049, China
[b] Institute of Geomechanics and Underground Technology, RWTH Aachen University, Mies-van-der-Rohe-Str. 1, 52074 Aachen, Germany
[c] State Key Laboratory of Nonlinear Mechanics, Institute of Mechanics, Chinese Academy of Sciences, Beijing, 100190, China
[d] School of Engineering Science, University of Chinese Academy of Sciences, 100049, China
[e] Shaanxi Key Laboratory for Vibration and Control of Aerospace Structures, School of Aerospace Engineering, Xi'an Jiaotong University, Xi'an, 710049, China

ARTICLE INFO

Article history:
Received 2 December 2022
Received in revised form 15 January 2023
Accepted 26 February 2023
Available online 5 March 2023

Keywords:
Flexoelectricity
Surface roughness
Contact stiffness
Electro-mechanical behavior

ABSTRACT

This study quantifies the role of surface roughness on interfacial flexoelectricity under normal compression and oscillation by examining a series of 3D-printed surfaces with diverse roughness features. For incipient contact, the measured flexoelectric charge is found to follow a power-law dependence on normal compression load, with the exponent positively correlated with the fractal dimension. The value of this power-law exponent is similar to that for contact stiffness. The underlying mechanism for this coincidence is elucidated by contact analyses based on geometric truncations of surface structures. Contact micromechanics show that the interfacial flexoelectric charge will increasingly concentrate on large microcontacts as the compression continues. A rougher surface with higher fractal dimension tends to demonstrate less heterogeneity for flexoelectric polarizations over microcontacts. This study provides systematic experimental measurements and comprehensive explanations for interfacial flexoelectricity and establishes quantitative links to multi-scale surface structures, shedding light on novel approaches for contact evaluation and flexoelectricity enhancement.

1. Introduction

Triboelectricity with interfacial charge transfer is ubiquitous in nature and engineering applications [1,2]. Extensive studies have been carried out to understand the mechanisms influencing electric charges and dipole moments. These mechanisms include flexoelectricity [3], chemical potential [4], temperature differences [5], electrostatic effects [6], trapped charges [7], etc. Among these, the flexoelectric effect, commonly existing in dielectric materials, has attracted increasing attention due to the rapid development of novel electronic, electro-mechanical, and photovoltaic applications [8–10]. In the early 1960s, Kogan [11] reported that the electrostatic potential in crystals can be generated by non-uniform strain and first proposed the concept of flexoelectricity. Flexoelectricity in dielectric materials describes the electric polarization induced by strain gradient, given by

$$P_l = \mu_{ijkl} \frac{\partial \varepsilon_{ij}}{\partial x_k} \tag{1}$$

where P_l, ε_{ij}, and x_k are the electric polarization, applied strain tensor, and position coordinate, respectively. The fourth-order tensor, μ_{ijkl}, represents the flexoelectric coefficient, defined as the production of the electric polarization vector and gradient of the second-order strain tensor [12]. Microscopically, non-uniform strain causes the offset between the equivalent positive and negative charge centers of deformed units and further results in polarization. Macroscopically, the polarization charges induced by strain gradient effectively accumulate on the surface electrode, thereby exhibiting potential variations [12]. Recent studies in flexoelectricity focus on decoupling flexoelectric coefficient components [13,14], polarization enhancement [15,16], length scale dependence [17,18], and advanced measurement methods for flexoelectricity in different structures and materials [19–22]. There are already various applications of flexoelectricity, including energy harvesting [23], monitoring crack growth [24], curvature measurement [25], quantification of thermally induced dynamic behavior [26], enhancement of acoustic gain [27], and controlling optoelectronic properties [28]. However, it is known

* Corresponding author at: Shaanxi Key Laboratory for Vibration and Control of Aerospace Structures, School of Aerospace Engineering, Xi'an Jiaotong University, Xi'an, 710049, China.
** Corresponding author.
E-mail addresses: liu.ky@xjtu.edu.cn (K. Liu), mlxu@xjtu.edu.cn (M. Xu).

https://doi.org/10.1016/j.eml.2023.101997
2352-4316/

that surfaces of material usually exhibit different behaviors compared to the bulk, and such difference largely originates from the surface roughness. Therefore, it is of great importance to systematically study the flexoelectricity at rough surfaces for better understanding, optimizing and collecting triboelectricity on natural and artificial surfaces presenting hierarchical structures.

The multi-scale structures featuring complex deformation of fractal rough surfaces lead to difficulties in understanding interfacial flexoelectricity [3,8,29]. By reanalyzing the Kelvin Force Microscopy data in [30], recent studies [29] pointed out that triboelectricity often results from flexoelectric, and the direction and magnitude of the surface potential differences were found to depend on the material properties, applied stresses, spatial distributions and shapes of contact asperities. At the microcontact level, classic Hertzian and JKR contact models were implemented for indentation and pull-off of nanoscale asperities against an elastic half-space, to attribute the yielded surface potential differences to contact flexoelectricity, proved by first-principles and finite element simulations [3,31]. With appropriate assumptions at specific length scales, analytical and numerical models for rough contacts are developed to depict the evolution of contact stiffness [32], adhesion effect [33], electrical and thermal conduction [34], and separation charge [29]. For small contact deformation, these widely-used multi-asperity contact models [35–38], in line with Greenwood and Williamson GW model [39], estimate the overall contact properties by integrating contact responses of individual asperities. During the integration process, the complexity induced by hierarchical surface roughness can be simplified by incorporating typical roughness parameters characterized with a cut-off frequency, such as mean surficial heights, root mean square roughness slope, mean asperity curvature, and asperity density, etc. For higher contact depths, Persson's theory [36] based on the concept of magnification is more frequently referred to. Moreover, Guo et al. [38] have proposed a model applicable over a wide range from low to high contact pressure with satisfactory calculation accuracy. Albeit these excellent progresses in analytical and numerical studies, it is widely admitted that tracking the overall contact area evolution, which is crucial in depicting interfacial electro-mechanical behavior, is still challenging in experiments.

Extensive experiments have been carried out to investigate the role of surface structure on interfacial behavior [34,40,41], but studies for the influence of surface roughness on interfacial flexoelectricity have seldom been reported. At the nanoscale, the Atomic Force Microscope (AFM) tip of several tens of nanometers has recently proven to be a reliable approach to exploit the unique features of surface flexoelectricity [42]. Kelvin force microscopy (KFM) was used to image surface potential over various polymer surfaces to investigate the charge distributions after contact electrification [43]. Macroscopically, the electric charge, converse flexoelectric effect, and impedance analysis have been employed to obtain flexoelectric coefficients of deformed solids, such as polymers [44], ceramics [45], non-oriented liquids [46], etc. Challenges for capturing the flexoelectric charge come from multiple aspects, including decoupling flexoelectric coefficient components [22], stably exporting the flexoelectric signal with a high signal-to-noise ratio [12], isolating flexoelectric effects from piezoelectric, electromagnetic, and electrostatic behavior [8]. Depending on the direction of generated strain gradient, there are longitudinal, transverse, and shear types of flexoelectricity. The truncated pyramid compression method has been used to investigate the longitudinal flexoelectric [47,48]. The bending beam method was developed to test the transverse flexoelectricity in ferroelectrics [49]. By twisting the cylinder structure, the shear flexoelectric component in polymeric materials has been evaluated [13,22]. To ensure measurement reproducibility and accuracy, dynamic loadings are commonly used [22,50]. It is worth emphasizing that measured values are often effective flexoelectric coefficients for polymer materials, which do not represent specific crystalline directions. This is because the deformation in polymer, unlike inorganic crystals in which elastic and plastic strains can be clearly defined, is more complicated and cannot be directly related to the chemical bonding configurations [15,22,48].

To figure out the relationship between interfacial flexoelectric and surface roughness, we measure interfacial flexoelectric charges at a series of 3D-printed rough surfaces presenting distinct geometrical features with carefully designed experiments. To elucidate the micromechanics, we provide a comprehensive numerical explanation to quantify the interfacial flexoelectricity at incipient contact. By combining the experimental and numerical results, the interfacial flexoelectricity is quantitatively connected to contact morphology and mechanical properties.

2. Materials and methodology

2.1. Sample characterizations

Surface geometric structures are essential in determining how contacting solids induce strain gradients and electric polarizations. To gain insights into the role of surface roughness on interfacial flexoelectric effects, a series of rough surfaces exhibiting distinct geometries are experimentally tested. This study employs two crucial surface descriptors controlling surface geometries, i.e., fractal dimension and roughness amplitude, which dominate, respectively, the hierarchical features and height scaling. Fractal rough surfaces consisting of 12 000 $\times$ 12 000 pixels are numerically generated and 3D-printed on a projective area of 12 mm $\times$ 12 mm, with fractal dimension, D_{in}, ranging from 2.1 to 2.9, and the roughness amplitude, R_t, ranging from 0.25 mm to 1.25 mm. Typical rough surfaces are shown in Fig. 1a. More details for surface generation and 3D printing are provided in Sec. A of Supplementary Material. Roughness characteristics, including conventional roughness parameters and fractal dimension, are provided in Table 1. Values of standard deviation shown in Table 1 are calculated based on ten realizations. In this study, the roll-off wavelength, L_r, and cut-off wavelength, L_c, corresponding to the left and right edges of the shaded area in Fig. 1b for the surface power spectra over spatial frequencies [35,51]. Here, L_r and L_c are, respectively, set to be 1.65 mm and 32 μm, as is detailed in Sec. A of Supplementary Material. The target roughness amplitude, R_t, representing the peak–valley height, is obtained by scaling height values of all pixels. Root mean square roughness, R_{rms} is calculated by $R_{rms} = \sqrt{\frac{1}{N}\sum_i^N z_i^2}$, where z_i is the height deviation from the mean plane, equivalent to the integration of surface power spectra from roll-off wavelength to cut-off wavelength [52].

Fractal dimension of generated surfaces can be evaluated using different methods, including the vertical sections method [53], power spectrum analysis [54], triangulation method [55], and box-counting method [56], etc. The output fractal dimensions, D_{out}, quantified by different methods are found to differ from each other, but in general, a larger D_{in} leads to a larger D_{out}. Values of D_{sp} and D_{vs} calculated, respectively, by power spectrum analyses and vertical sections method are compared in Table 1. To thoroughly compare the five types of surfaces, we provide their power spectra over spatial frequency (Fig. 1b), relations between the total perimeter and the total area of all truncation spots (Fig. 1c), and the number of truncated spots at various truncation heights (Fig. 1d).

Power-law relations can be seen in both Fig. 1b and c, and the exponent values are used to determine the fractal dimension. Specifically, the continuous power spectrum for a fractal rough

Table 1
Characteristics of surface roughness.

Sample	R_t (mm)	R_{rms} (μm)	D_{in}	D_{sp}	D_{vs}	T_{dep}^{peak}	C_{dep}^{edge}
S1	0.75	135.61 ± 8.73	2.10	2.16 ± 0.03	2.13 ± 0.02	29.72% ± 1.23%	25∼35%
S2	0.75	124.64 ± 10.28	2.30	2.36 ± 0.03	2.40 ± 0.03	30.45% ± 1.76%,	25∼35%
S3	0.75	111.13 ± 5.75	2.50	2.49 ± 0.03	2.55 ± 0.03	30.83% ± 1.14%	25∼35%
S4	0.75	103.99 ± 7.04	2.70	2.67 ± 0.02	2.72 ± 0.02	32.36% ± 1.58%	30∼40%
S5	0.75	88.11 ± 3.48	2.90	2.81 ± 0.04	2.84 ± 0.02	33.96% ± 1.63%	35∼45%
S6	0.25	38.41 ± 1.42	2.50	2.48 ± 0.04	2.57 ± 0.02	31.77% ± 1.89%	25∼35%
S7	0.50	77.95 ± 5.03	2.50	2.49 ± 0.03	2.55 ± 0.03	32.28% ± 1.17%	30∼40%
S8	1.00	149.82 ± 11.48	2.50	2.48 ± 0.04	2.55 ± 0.04	30.96% ± 1.43%	30∼40%
S9	1.25	182.91 ± 11.57	2.50	2.48 ± 0.04	2.56 ± 0.03	32.32% ± 1.39%	30∼40%

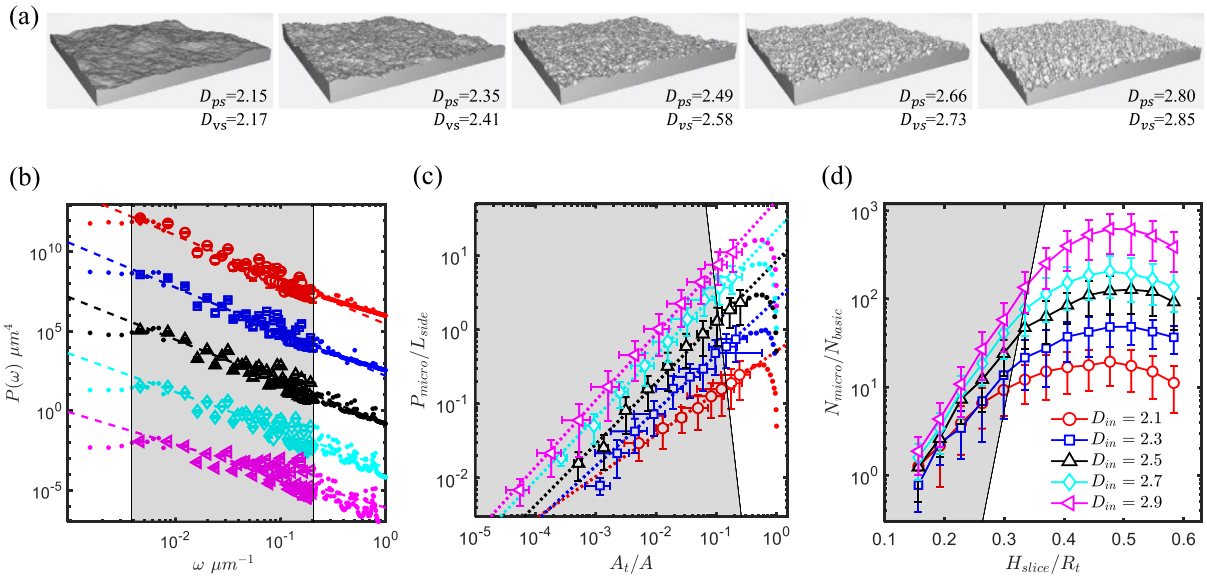

Fig. 1. Surface geometry analyses: (a) typical rough surfaces demonstrating various hierarchical structures with the roughness amplitude of 0.75 mm. Calculated values of fractal dimension using power spectrum analysis and vertical sections method are provided at the right-bottom of each subfigure. (b) Power spectra over spatial frequencies; (c) relations between the normalized total perimeter, P_{micro}/L_{side}, and area, A_t/A for all truncation spots, and (d) the normalized number of truncated spots, N_{micro}/N_{basic}, at various truncation depths, H_{slice}/R_t. Here, L_{side} is the side length of the sample, and $N_{basic} = A/L_r^2$ is calculated as the ratio between the nominal area and the square of roll-off wavelength. Dashed lines in (b) and (c) are fitted curves based on data within the shaded areas. The left and right edges of (b) correspond to the roll-off frequency and cut-off frequency, respectively. Right edges of (c) and (d) correspond to the maximum increasing rate of micro-spots numbers as the truncation deepens. Error bars in (b)–(d) are based on ten realizations. Subfigures (b)–(d) share the same legend in (d).

surface, $P(\omega)$, can be approximated by $P(\omega) = 1/\omega^{(7-2D_{ps})} \ln\gamma$, which is an inverse power function of the spatial angular frequency, ω [35,54]. Only data included in the shaded area is employed in curve fitting with the left and right edges, corresponding to the roll-off and cut-off frequencies, respectively. The correlation between P_{micro} and A_t summed over all micro spots can be approximated by $P_{micro} \propto A_t^{(D_{vs}-1)/2}$, as shown in the shaded area of Fig. 1c. The right edge of the shaded area in Fig. 1c and d are determined by the fitted curve with points of critical truncation depth, T_{dep}^{peak}, listed in Table 1. Here, T_{dep}^{peak} corresponds to the depth with the highest increasing rate of the number of truncation spots as the truncation deepens. In fact, the linear relationship between P_{micro} and A_t in log–log plots can be further extended to around $0.3A_t/A$, corresponding to peaks values near $0.5H_{slice}/R_t$ in Fig. 1d. This suggests the number of truncation spots reaches a maximum increasing rate before the total perimeter of all spots reaches the peak, after which the merging of micro spots tends to dominate the area evolution [53,56].

2.2. Experimental setup

To ensure measurement accuracy and reliability, we take particular consideration of the synchronization of measured flexoelectric charge and contact stiffness, isolation of the flexoelectric effects from other piezoelectric, electromagnetic, and electrostatic effects, and the improvement of signal-to-noise ratio. The interfacial flexoelectric charges of 3D printed rough surfaces are examined with the experimental setup shown in Fig. 2b. The tested rough surface is sandwiched by two stainless steel electrodes, which are well polished demonstrating R_t of 1.56 ± 0.73 μm and R_{rms} of 0.092 ± 0.005 μm, averaged over ten scans of 1 × 1 mm^2 using the profilometer (Type 1000WLI, NanoMap). Considering the R_t range of 3D printed surfaces, the stainless-steel platen can be deemed perfectly flat here. A thin layer of carbon conductive grease (Type 846, MG Chemicals) is painted between the bottom electrode and the tested sample. The interfacial gap between the top electrode and the rough surface structure is filled with the conductive grease to isolate the flexoelectric effect during the measurement. The compression and oscillation are applied by the micro tester, Instron 5848. Apart from the built-in measurement units, the deformation and force are further examined, respectively, by the camera of Basler acA2440, and the force sensor of HBM S9M (2 kN) together with the signal processor HBM AB22A. Image correlations are conducted in Matlab environment for recorded images (20 frames/s) focusing on the distance between the top and bottom electrodes, to extract the oscillation displacement with the accuracy higher than 0.1 μm. In the test, the prescribed compression F_c is applied to realize apparent contact pressure (F_c/A, where A is the projected area of the tested surface) ranging from 0.034 to 8.89 MPa. When each compression F_c is stable, the sinusoidal oscillation with the varying F_c from $0.95F_c$ to $1.05F_c$ at low frequencies (<2 Hz) is

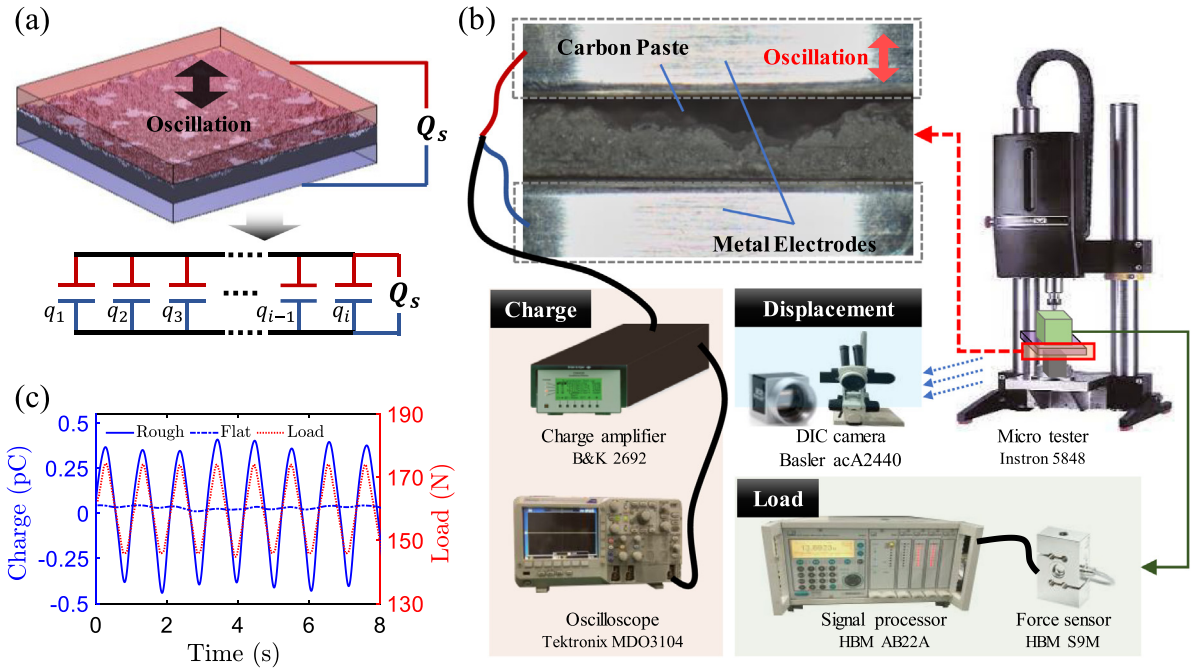

Fig. 2. (a) Schematic of the flexoelectric effect of a fractal rough surface under normal compression and oscillation. (b) The experimental setup for measuring the contact load, deformation, and interfacial charge of a rough surface under normal compression and oscillation. (c) The typical output charge measured for sample S7 under the normal compression of 160 N and the oscillation of 1 Hz and 16 N in magnitude. With the same loading condition, the measured electrical charge of the reference surface of the 3D-printed cube in 2 mm × 12 mm × 0.5 mm, is provided in the blue dashed line.

imposed. Note that the yield strength of the used 3D-printing material is approximately 49 MPa. During the oscillation, the probed electric charge from the specimen is amplified and recorded. The charge amplifier, B&K 2692, is employed with the amplification of 1 V/pC, converting the captured charge into the voltage signal. The amplified signal is then recorded using the oscilloscope of Tektronix MDO3104 for further analysis. Shield wires are used for high-quality signal transmission. After the test, the variations of surface roughness for both specimens and electrodes are quantified, as detailed in Sec. E of Supplementary Material.

To prevent pyro-electric effects, only oscillations with frequencies less than 2 Hz is employed in this study. The typical oscillation amplitude is one-tenth of the corresponding compression level to maintain linearity between the contact force and deformation during oscillation. The contact stiffness is estimated by the mean slope of the roughly linear load–deformation curves over oscillation cycles. At a given compression level, the applied oscillation includes 20 cycles, and only the last ten cycles presenting the higher signal-to-noise ratio are used to calculate contact stiffness and flexoelectric charge. Additionally, a digital lowpass filter with a cut-off frequency of 5 Hz is used to remove noises of high frequencies. One typical filtered real-time waveform of the electric charge output of a tested sample is provided in Fig. 2c. Note that the flat surface of the 3D-printed cube for reference is evaluated by the profilometer (Type 1000WLI, NanoMap), exhibiting $R_t = 5.65 \pm 0.49$ μm and $R_{rms} = 0.98 \pm 0.07$ μm, averaged over ten scans of 1 × 1 mm^2. In this study, the piezoelectric effect is ignored due to the use of dielectric materials. Moreover, to isolate the flexoelectric charge and mitigate the influences of other mechanisms, we proposed to fill carbon conductive grease in the interfacial gap to force the electric potential of the whole rough surface to be equal to that of the top electrode, and to avoid direct contact and separation between the electrodes and the rough surface.

3. Theory

The overall flexoelectric charge of the compressed rough surface is collectively contributed by all contacting asperities, each of which can be regarded as an individual charge source in parallel with others. The applied normal compression on an asperity of dielectric materials will yield concentrated stress at the tip region, exhibiting sharp strain gradients due to the irregularity of the asperity shape, thus inducing contact flexoelectricity. Here, we implement a concise self-consistent model for the contact of inelastic materials [57], based on the indentation theory [58] and von Mises isotropic flow theory [59]. For an elastoplastic frictionless contact problem of an asperity under normal compression, the constitutive behavior can be simplified as

$$f_i = a_i\sigma_i = a_i E_r \varepsilon_i = \pi {r_i}^2 E_r \alpha \left(\frac{\beta r_i}{2R_i}\right)^{m_B} \tag{2}$$

where $\alpha = 3$ and $\beta = 1/3$ are universal geometric constants, m_B is hardening exponent, with $m_B = 0$ for a perfectly plastic case, and $m_B = 1$ for a linearly elastic case, and r_i and R_i are, respectively, the effective microcontact radius and effective radius of the asperity tip [60]. The composite modulus, E_r, is contributed by materials of both contact pairs, given by $1/E_r = \left(1-\upsilon_1^2\right)/E_1 + \left(1-\upsilon_2^2\right)/E_2$, with E and υ being the material Young's modulus and Poisson's ratio, respectively, and the subscript 1 and 2 indicating the materials of contacting surface. The overall contact force, F_c can be obtained by integrating all contacted asperities, $\sum f_i$, where i means the ith contact asperity.

When an oscillation of small amplitude is applied on the compressed surface, the induced contact deformation and the effective contact strain can be considered to be inversely proportional to the normal contact stiffness, K_c. In this study, K_c is calculated by $\mathrm{d}F_c/\mathrm{d}d$, with d being the contact depth approximated by the truncation depth, as is adopted in [32,61,62]. The authors are aware that our definition of contact stiffness differs from the definition in indentation-type experiments [58],

where contact stiffness refers to the unloading regime, governed exclusively by elasticity. However, in our experiments, the magnitude of the oscillation is small that the unloading regime is difficult to capture. Therefore, we define the contact stiffness to be the derivative of the contact force–displacement curve for convenience (and we also expect that such a definition will not differ much from the indentation stiffness when the surface mainly deforms elastically) and keep the definition consistent in both experiments and numerical modeling such that they are qualitatively comparable.

According to Eq. (1), the flexoelectric polarization for an individual microcontact, p_i, can be effectivity calculated by

$$p_i = \mu_{eff} \frac{\Delta\varepsilon_{a_i}}{T_s} \tag{3}$$

where μ_{eff} is the effective flexoelectric coefficient, mainly contributed by the longitudinal component of μ_{ijkl}, T_s is the distance between the top and bottom electrodes, and $\Delta\varepsilon_{a_i}$ is the variation of the contact strain at the tip of ith microcontact. Meanwhile, the electric polarization can also be calculated by

$$p_i = \frac{q_i}{a_i} \tag{4}$$

where q_i is the exported flexoelectric charge at ith microcontact, and a_i is the microcontact area. Combining Eqs. (3) and (4), the interfacial flexoelectric charge, Q_s, can be integrated by the polarization at each individual microcontact

$$Q_s = \sum_i^{N_{micro}} a_i p_i = \frac{\mu_{eff}}{T_s} \sum_i^{N_{micro}} a_i \Delta\varepsilon_{a_i}. \tag{5}$$

In this study, truncation areas at various surface heights are used to approximate the real contact area for i-th individual microcontact area, a_i, and the overall surface contact area, $A_c = \sum a_i$. This approximation has been employed by a number of previous studies [32,35,56,61]. In fact, for normal compression at incipient contact, the contact strain is confined within the asperity tip region rather than the bulk region, wherein contacting asperities tend not to interact with each other. Under further compression, occurring asperity interactions, asperity breakage, debris piling, and bulk failure could potentially lead to limitations in using the geometric truncation to account for the real contact area. The maximum truncation depth for applying this approximation to determine contact stiffness is found to be around one-third to half of the roughness amplitude, as discussed by [56]. Additionally, the implemented numerical approach for estimating interfacial electro-mechanical behavior can be affected by the spatial resolution of simulated surfaces and increment steps of truncation depth. The resolution of 12 000 × 12 000 pixels over the area of 12 mm × 12 mm and 300 increment steps (with the maximum truncation depth up to $T_{dep}^{max} = 1/2R_t$) are used to ensure numerical convergence. Here, we only show main equations and more details regarding the numerical procedures for extracting the interfacial flexoelectric charge are provided in Sec. B of Supplementary Material.

4. Results and discussion

4.1. The role of surface roughness

Experimental and numerical results shown in Fig. 3 suggest both interfacial flexoelectric charges and contact stiffness demonstrate power-law dependences on the normal compression, which can be, respectively, described by $Q_s = \beta_e[F_c/(EA)]^{\alpha_e}$ and $K_c/\left(E\sqrt{A}\right) = \beta_k[F_c/(EA)]^{\alpha_k}$. The roughness amplitude is found to govern the magnitude parameters β_k and β_e, and exponent values of α_k and α_e strongly correlate with surface fractality. Values of α_k and α_e are barely affected by the small and slow oscillations applied in present experiment, which are capable of steadily exporting flexoelectric charges without introducing significant non-linear behavior. To ensure the proper oscillation parameters, we examine the influence of the oscillation load, amplitude, and frequency on the measurement, as is detailed in Sec. C of Supplementary Material. Obtained α_k values in this study are comparable to those of previous numerical and experimental studies [56,63], validating the proposed numerical approach. Additionally, the direct use of the longitudinal coefficient, μ_{11} for approximating μ_{eff} in conducted simulations could be one important reason for having the interfacial flexoelectric charge overestimated. The value of μ_{11} is estimated based on the macroscopic compression test for a truncated cone, as detailed in Sec. D of the Supplementary Materials. The obtained μ_{11} reflects only effective properties, which may consist of various flexoelectric contributions and combine multiple flexoelectric tensor components [8,13,14,22,50].

For experimental measurements, power-law fittings are conducted only for compression ranges covered by gray shaded areas. The right edge of the shaded area is selected based on the fact that the contact stiffness with higher compression levels tends to converge across different samples, presenting clear divergence from the power law scaling. The selected right edge corresponds to a compression load P_{dep}^{edge} of about 2 MPa, resulting in the contact deformation, C_{dep}^{edge}, of around 25% to 40% of R_t for different specimens, as is listed in Table 1. Here, only a rough range is given based on accumulated contact deformation over loading steps. Small variations of measured deformation before and after the applied oscillations can be observed, indicating the contact of contact status with possible asperity yielding and breakage. To quantify the influences of compression and oscillation on surface structures, we examine the change of roughness amplitude before and after mechanical loadings, as is detailed in Sec. E of the Supplementary Material. The considered surfaces are only slightly modified for incipient contacts with compression loads up to P_{dep}^{edge}. In contrast, the compression of 8.89 MPa can yield significant modifications of surface structures, possibly accompanied by asperity breakages and bulk failures. As is further compared in Table 1, ranges of C_{dep}^{edge} are found to be able to cover T_{dep}^{peak} extracted from numerical calculations. Nevertheless, this coincidence suggests the applicability of the proposed numerical approach.

Interestingly, power-law scalings for flexoelectric charge and contact stiffness demonstrate similar exponent values for a given surface structure, as is compared in Fig. 5b. At small loading, when elastic deformation dominates, according to indentation theory [58], the contact stiffness can be related to the real contact area through $K_c = \beta_c \frac{2}{\sqrt{\pi}} E_r \sqrt{A_c}$, where E_r is the reduced Young's modulus, β_c is a geometrical constant on the order of unity [58]. We then obtain the scaling relationship of $K_c \propto \sqrt{A_c}$. On the other hand, Eq. (5) suggests the measured interfacial charge follows the relationship of $Q_s \propto \sum a_i \Delta\varepsilon_{a_i}$. For a given oscillation, the contact strain is essentially determined by the contact deformation that is inversely proportional to the contact stiffness, K_c. Consequently, the scaling of $Q_s \propto A_c/K_c \propto \sqrt{A_c}$ would hold to some extent. In a sense, both Q_s and K_c are positively correlated with $\sqrt{A_c}$. Though not sufficiently rigorous in terms of the evolution of complex rough structures and occurring nonlinearity in contact behavior, these simple scaling analyses provide a plausible point to interpret the interfacial flexoelectricity at fractal rough surfaces, highlighting the role of the real contact area. Actually, other interfacial quantities, including electrical contact resistance, capacitance, and thermal conductance present similar power-law scaling with respect to applied loads, mainly for low to medium

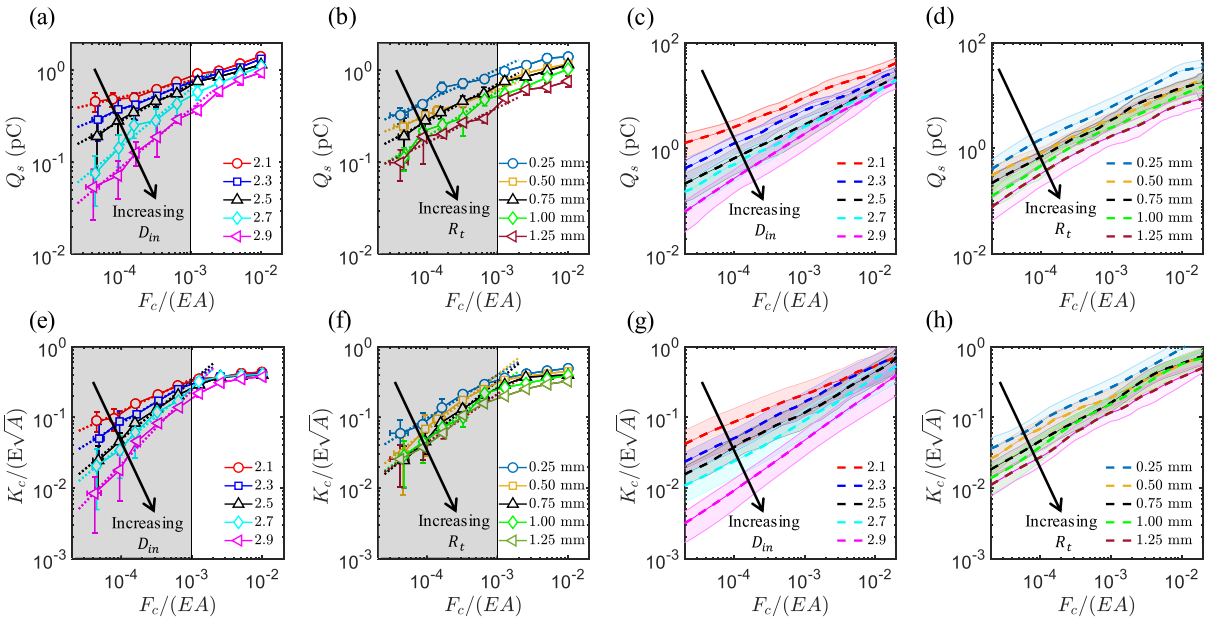

Fig. 3. Experimental and numerical results for flexoelectric charge and contact stiffness. For flexoelectric charge, results for various fractal dimensions are shown in (a) and (c) for experiments and simulations, respectively. Results for various roughness amplitudes are shown in (b) and (d) for experiments and simulations, respectively. For contact stiffness, results for various fractal dimensions are shown in (e) and (g). Results for various roughness amplitudes are shown in (f) and (h), for experiments and simulations, respectively. The normalization procedures are applied for contact stiffness by $K_C/\left(E\sqrt{A}\right)$ and for applied load by $F_c/(EA)$, with E being Young's modulus of the tested material, and A the apparent contact area. For experimental results, error bars are calculated over ten measurements, and dotted lines are fitted curves using mean data points within the gray shaded area. For numerical results, shaded areas of standard deviations are obtained over ten realizations, while dashed lines follow the mean data points.

compression levels. The contact area turns out to be the pivotal parameter to quantify and unify them. The question remains on quantitatively estimating the contact area, the interfacial void, and any other structural characteristics, which depends on fine and extremely fine details. The fractality shown by the hierarchical surface structures may become less important with decreasing length scale in determining interfacial mechanical interaction, electron transport, heat transfer, etc. This can be generally supported by experimental studies on contact stiffness [32,56,61,63], electrical contact resistance [34], heat conduction [64], friction [40,65], and interfacial flexoelectricity [29,31], etc.

4.2. Contributions of contact patches to interfacial flexoelectric charges

A rougher surface is featured with increasing structure randomness and hierarchies displaying finer details. Reduced dimensions potentially imply larger strain gradients, suggesting flexoelectricity would possibly be more significant at smaller length scales, which presents smaller contact patches. One could intuitively reckon that a rougher surface would demonstrate a more significant flexoelectric charge. However, one should also note that the resultant flexoelectric charge is the product of the flexoelectric polarization (which is proportional to the strain gradient) and the contact area. Ideally, on the one hand, when the surface roughness is high (which would result in a very large flexoelectric polarization), the contact area tends to be zero since the contact patches would be needle-like; on the other hand, when the surface roughness is low (such as a flat surface), the contact patch area is large, but the flexoelectric polarization tends to be zero, such as the reference test shown in Fig. 2c. Therefore, the flexoelectric charge at the rough interface is a complex problem that involves not only initial surface topography but also the contact evolution which strongly relates to again surface topography and mechanical properties. For the rough surfaces examined in this study, results show that a rougher surface tends to yield a lower flexoelectric charge than a smoother surface under the same loading condition. In Fig. 4, we provide the joint histogram for microcontact strain variation, $\Delta\varepsilon_{a_i}$, and microcontact areas, a_i/A. The former governs flexoelectric polarization, as shown in Eq. (3), and the latter represents the electrode area for microcontacts. First of all, it can be seen that for different surfaces under varying loading conditions, strong correlations between $\Delta\varepsilon_{a_i}$ and a_i/A can be observed with correlation coefficients usually larger than 0.7. This observation indicates larger microcontacts also tend to exhibit larger strain variations, thus larger flexoelectric polarization contributing more to the interfacial flexoelectric charge. For a given loading condition, both $\Delta\varepsilon_{a_i}$ and a_i/A are found to be scattered over narrowing ranges as the fractal dimension increases, as is compared in each row of Fig. 4. Moreover, their respective mean values of $\Delta\varepsilon_{a_i}$, marked by horizontal dotted lines, are found to show decreasing trends with the fractal dimension. It can be seen that for surfaces with lower D_{in}, there are more big microcontacts (this can also be seen through the mean values of $\Delta\varepsilon_{a_i}$). This naturally explains a lower D_{in} results in a higher flexoelectric charge, as shown in Fig. 3.

To quantify the contribution of microcontacts of different sizes to the overall interfacial flexoelectric charge, we examine the Gini coefficient, f_{gini}, for the produced flexoelectric polarization by individual microcontact. The Gini coefficient is often used to represent inequality of some quantity in a population. Such a coefficient of unity indicates complete inequality; meanwhile, a value of 0 indicates perfect equality and homogeneity. Here, we order all flexoelectric charges of individual microcontact, calculated by $p_i = a_i p_i$, at a given truncation height in nondecreasing order ($q_i \leq q_{i+1}$) and compute f_{gini} by $f_{gini} = \frac{1}{N_{micro}}\left\{N_{micro} + 1 - 2\left[\frac{\sum_{i=1}^{N_{micro}}(N_{micro}+1-i)q_i}{\sum_{i=1}^{N_{micro}} q_i}\right]\right\}$. For all surfaces of different fractal dimensions, we observe the monotonic increase of the Gini coefficient with contact deformation, suggesting the yielded interfacial flexoelectric charge becomes more heterogeneous with increasing compression. For a given contact

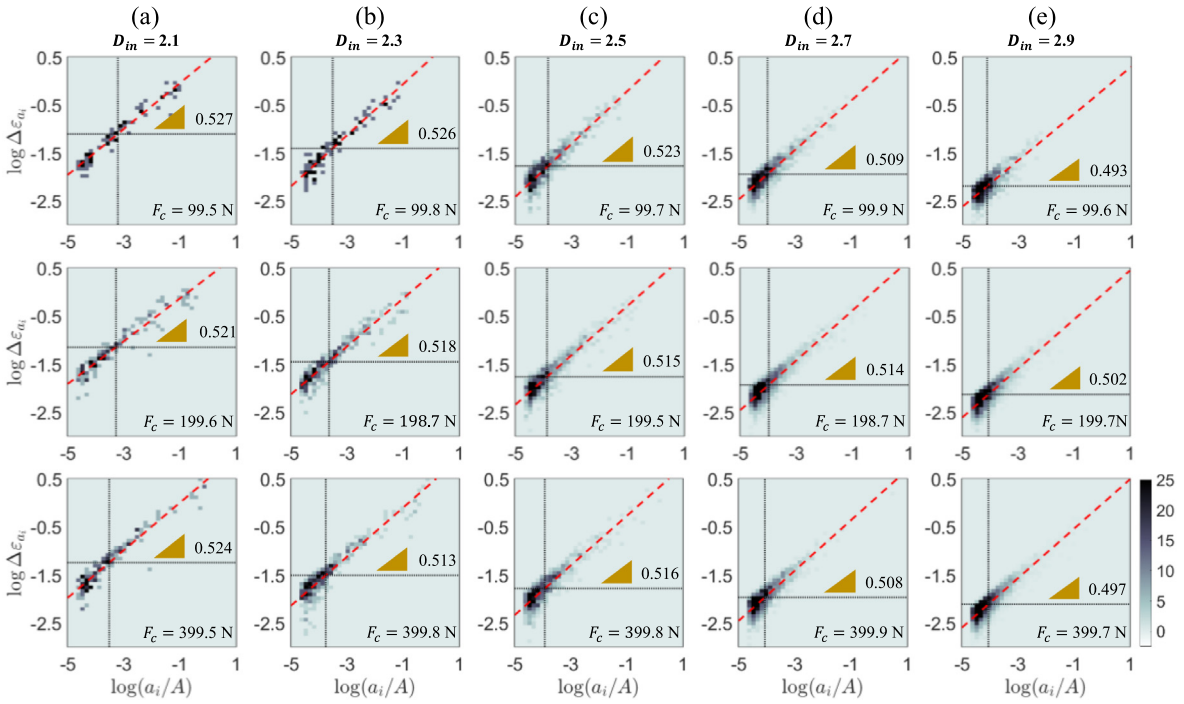

Fig. 4. Joint histograms for the microcontact strain variation, $\Delta\varepsilon_{a_i}$, and normalized microcontact area, a_i/A, for rough surfaces with different D_{in} of 2.1 (a), 2.3 (b), 2.5 (c), 2.7 (d), and 2.9 (e), respectively. The microcontact strain variation, $\Delta\varepsilon_{a_i}$ is the difference of asperity strain extracted between $1.05F_c$ and $0.95F_c$. The first, second, and third rows correspond to different normal compressions of about 99.5 N–100 N, 199.5 N–200 N, and 399.5 N–400 N, which are provided at the right-bottom corner of subfigures. The dashed lines indicate fitted curves, and their slopes are shown beside the corresponding triangle. The horizontal and vertical dotted lines indicate the average values of asperity contact strain variations and microcontact areas.

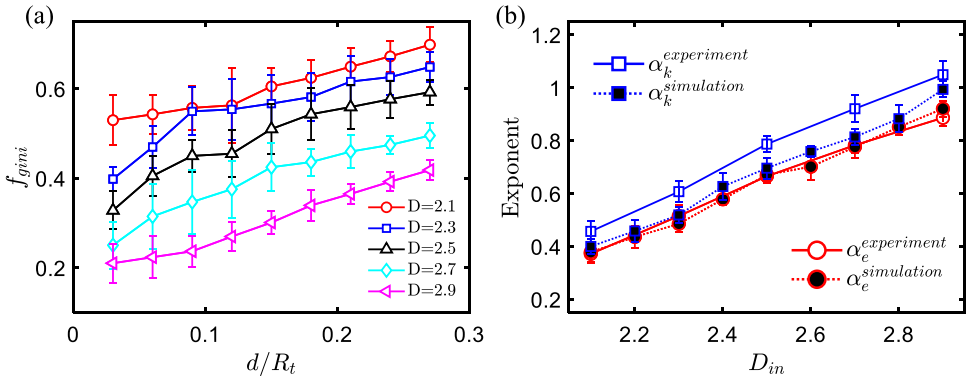

Fig. 5. (a) Gini coefficients of flexoelectric charges produced by individual microcontacts for varying contact deformation. (b) Exponent values of power-law dependences of flexoelectric charge and contact stiffness on normal compression, for surfaces of S1-5. Error bars show the corresponding standard deviations calculated from ten realizations.

deformation, surfaces with lower D_{in} values show higher Gini coefficients, demonstrating that the exported contact flexoelectric charges tend to be dominated at large microcontacts, as is further supported by results in Fig. 4. These findings are essential in our ongoing studies for programming interfacial flexoelectricity by properly constructing multi-scale surface textures and designing loading paths.

5. Conclusions

This study provides a systematic experimental investigation on the interfacial flexoelectric charge with a series of 3D-printed fractal rough surfaces under normal compression and oscillation. A numerical framework based on truncation analyses is proposed to comprehensively interpret experimental observations. Through the comparison between experimental and numerical results, parametric analyses, and asperity micromechanics, the following conclusions can be drawn:

(1) A unified power-law function exists between the interfacial flexoelectric charge and normal compression. The power-law exponent increases with the fractal dimension, while the power-law scaling magnitude decreases with the roughness amplitude.

(2) The power-law exponent for the interfacial flexoelectric charge is comparable to that for the normal contact stiffness. This similarity can be traced to the evolution of contact area under increasing compression, which is the primary determinant for both contact behavior.

(3) The interfacial flexoelectric charge will increasingly concentrate on large microcontacts as the compression increases. A smoother surface with a lower value fractal dimension tends to demonstrate more significant heterogeneity in the distribution of flexoelectric charges over microcontacts.

The present experiments and numerical explanations provide an essential step towards connecting interfacial electro-mechanical properties and multi-scale surface structures, providing supplementary data and guidelines for quantification of contact status, design of interfaces with enhanced electro-mechanical couplings, and development of non-destructive tools for evaluating rough contacts.

CRediT authorship contribution statement

Chongpu Zhai: Conceptualization, Methodology, Original draft preparation. **Shuwen Zhang:** Conceptualization, Writing – review & editing. **Hui Ji:** Experimental measurements, Data analysis, Reviewing, Editing. **Deheng Wei:** Theoretical analyses, Writing – review & editing. **Hengxu Song:** Theoretical analyses, Reviewing, Editing. **Kaiyuan Liu:** Conceptualization, Reviewing, Editing. **Minglong Xu:** Supervision, Funding acquisition, Writing – review & editing.

Declaration of competing interest

The authors declare that they have no known competing financial interests or personal relationships that could have appeared to influence the work reported in this paper.

Data availability

No data was used for the research described in the article.

Acknowledgments

This study is supported by No. LX6J018 and No. XZY012021003 from Xi'an Jiaotong University, China. The authors also gratefully acknowledge the financial support by the National Science Foundation of China under No. 12202342.

Appendix A. Supplementary data

Supplementary material related to this article can be found online at https://doi.org/10.1016/j.eml.2023.101997.

References

[1] S. Pan, Z. Zhang, Fundamental theories and basic principles of triboelectric effect: A review, Friction 7 (1) (2019) 2–17.
[2] C. Wu, et al., Triboelectric nanogenerator: a foundation of the energy for the new era, Adv. Energy Mater. 9 (1) (2019) 1802906.
[3] C.A. Mizzi, A.Y. Lin, L.D. Marks, Does flexoelectricity drive triboelectricity? Phys. Rev. Lett. 123 (11) (2019) 116103.
[4] S. Wang, et al., Molecular surface functionalization to enhance the power output of triboelectric nanogenerators, J. Mater. Chem. A 4 (10) (2016) 3728–3734.
[5] B. Cheng, et al., High performance temperature difference triboelectric nanogenerator, Nature Commun. 12 (1) (2021) 1–8.
[6] N. Balke, et al., Exploring local electrostatic effects with scanning probe microscopy: implications for piezoresponse force microscopy and triboelectricity, ACS Nano 8 (10) (2014) 10229–10236.
[7] H. Jiang, et al., Charge-trapping-blocking layer for enhanced triboelectric nanogenerators, Nano Energy 75 (2020) 105011.
[8] B. Wang, et al., Flexoelectricity in solids: Progress, challenges, and perspectives, Prog. Mater. Sci. 106 (2019) 100570.
[9] Q. Deng, et al., The collusion of flexoelectricity and Hopf bifurcation in the hearing mechanism, J. Mech. Phys. Solids 130 (2019) 245–261.
[10] H. Guo, et al., Flexoelectricity in hexagonal boron nitride monolayers, Extreme Mech. Lett. 52 (2022) 101669.
[11] S.M. Kogan, Piezoelectric effect during inhomogeneous deformation and acoustic scattering of carriers in crystals, Sov. Phys.-Solid State 5 (10) (1964) 2069–2070.
[12] P. Yudin, A. Tagantsev, Fundamentals of flexoelectricity in solids, Nanotechnology 24 (43) (2013) 432001.
[13] K. Liu, et al., Decoupled shear flexoelectric effects in polymers, J. Appl. Phys. 125 (17) (2019) 174104.
[14] A. Li, B. Wang, S. Yang, On some basic aspects of flexoelectricity in the mechanics of materials, Internat. J. Engrg. Sci. 166 (2021) 103499.
[15] H. Ji, et al., Flexoelectric enhanced film for ultrahigh tunable piezoelectric-like effect, Mater. Horiz. (2022).
[16] S. Sharma, et al., Strategies to instigate superior electromechanical response in dielectric materials via converse flexoelectricity, Extreme Mech. Lett. 42 (2021) 101138.
[17] A. Yurkov, P. Yudin, Continuum model for converse flexoelectricity in a thin plate, Internat. J. Engrg. Sci. 182 (2023) 103771.
[18] V.A. Eremeyev, et al., Flexoelectricity and apparent piezoelectricity of a pantographic micro-bar, Internat. J. Engrg. Sci. 149 (2020) 103213.
[19] K. Lefki, G. Dormans, Measurement of piezoelectric coefficients of ferroelectric thin films, J. Appl. Phys. 76 (3) (1994) 1764–1767.
[20] J. Hong, D. Vanderbilt, First-principles theory and calculation of flexoelectricity, Phys. Rev. B 88 (17) (2013) 174107.
[21] P. Zubko, G. Catalan, A.K. Tagantsev, Flexoelectric effect in solids, 2013.
[22] S. Zhang, et al., Investigation of the 2312 flexoelectric coefficient component of polyvinylidene fluoride: Deduction, simulation, and mensuration, Sci. Rep. 7 (1) (2017) 1–9.
[23] Q. Deng, et al., Nanoscale flexoelectric energy harvesting, Int. J. Solids Struct. 51 (18) (2014) 3218–3225.
[24] J. Sladek, et al., Flexoelectric effect in dielectrics under a dynamic load, Compos. Struct. 260 (2021) 113528.
[25] X. Yan, et al., A sensor for the direct measurement of curvature based on flexoelectricity, Smart Mater. Struct. 22 (8) (2013) 085016.
[26] L. Chu, G. Dui, Y. Zheng, Thermally induced nonlinear dynamic analysis of temperature-dependent functionally graded flexoelectric nanobeams based on nonlocal simplified strain gradient elasticity theory, Eur. J. Mech. A Solids 82 (2020) 103999.
[27] M. Willatzen, et al., Acoustic gain in solids due to piezoelectricity, flexoelectricity, and electrostriction, Adv. Funct. Mater. 30 (39) (2020) 2003503.
[28] S.V. Kalinin, A.N. Morozovska, Focusing light on flexoelectricity, Nature Nanotechnol. 10 (11) (2015) 916–917.
[29] B. Persson, On the role of flexoelectricity in triboelectricity for randomly rough surfaces, Europhys. Lett. 129 (1) (2020) 10006.
[30] H. Baytekin, et al., The mosaic of surface charge in contact electrification, Science 333 (6040) (2011) 308–312.
[31] C.A. Mizzi, L.D. Marks, When flexoelectricity drives triboelectricity, Nano Lett. (2022).
[32] S. Jiang, Y. Zheng, H. Zhu, A contact stiffness model of machined plane joint based on fractal theory, 2010.
[33] M. Ciavarella, et al., The role of adhesion in contact mechanics, J. R. Soc. Interface 16 (151) (2019) 20180738.
[34] C. Zhai, et al., Interfacial electro-mechanical behaviour at rough surfaces, Extreme Mech. Lett. 9 (2016) 422–429.
[35] W. Yan, K. Komvopoulos, Contact analysis of elastic–plastic fractal surfaces, J. Appl. Phys. 84 (7) (1998) 3617–3624.
[36] B.N. Persson, Contact mechanics for randomly rough surfaces, Surf. Sci. Rep. 61 (4) (2006) 201–227.
[37] H. Ghaednia, et al., A review of elastic–plastic contact mechanics, Appl. Mech. Rev. 69 (6) (2017).
[38] X. Guo, B. Ma, Y. Zhu, A magnification-based multi-asperity (MBMA) model of rough contact without adhesion, J. Mech. Phys. Solids 133 (2019) 103724.
[39] J.A. Greenwood, J.P. Williamson, Contact of nominally flat surfaces, Proc. R. Soc. Lond. Ser. A 295 (1442) (1966) 300–319.
[40] B. Weber, et al., Molecular probes reveal deviations from Amontons' law in multi-asperity frictional contacts, Nature Commun. 9 (1) (2018) 1–7.
[41] T.D. Jacobs, A. Martini, Measuring and understanding contact area at the nanoscale: a review, Appl. Mech. Rev. 69 (6) (2017).
[42] S.M. Park, et al., Flexoelectric control of physical properties by atomic force microscopy, Appl. Phys. Rev. 8 (4) (2021) 041327.
[43] E. Lorenzett, et al., Flexoelectric characterization of dielectrics under tensile, compressive, and flexural loads by non-contact Kelvin probe measurements, J. Appl. Phys. 129 (20) (2021) 204502.
[44] S. Baskaran, et al., Experimental studies on the direct flexoelectric effect in α-phase polyvinylidene fluoride films, Appl. Phys. Lett. 98 (24) (2011) 242901.
[45] P. Zubko, et al., Strain-gradient-induced polarization in SrTiO 3 single crystals, Phys. Rev. Lett. 99 (16) (2007) 167601.
[46] S. Zhang, et al., Flexoelectricity in non-oriented liquids, J. Phys. D: Appl. Phys. 54 (6) (2020) 06LT01.
[47] M. Zhang, et al., Ultrahigh flexoelectric effect of 3D interconnected porous polymers: modelling and verification, J. Mech. Phys. Solids 151 (2021) 104396.
[48] H. Ji, et al., Giant flexoelectric response via mechanical and material design in elastomers, Mech. Mater. 165 (2022) 104186.

[49] W. Ma, L.E. Cross, Observation of the flexoelectric effect in relaxor Pb (Mg 1/3 Nb 2/3) o 3 ceramics, Appl. Phys. Lett. 78 (19) (2001) 2920–2921.
[50] K. Liu, et al., Mechanical design of uniform strain-gradient schemes for transverse and longitudinal flexoelectricity, Int. J. Solids Struct. 238 (2022) 111414.
[51] M. Kanafi, Surface generator: artificial randomly rough surfaces, MATLAB Cent. File Exch. 15 (2016) Accessed September.
[52] D.S. Kammer, et al., The existence of a critical length scale in regularised friction, J. Mech. Phys. Solids 63 (2014) 40–50.
[53] B.B. Mandelbrot, D. Passoja, A.J. Paullay, Fractal character of fracture surfaces of metals, Nature 308 (5961) (1984) 721–722.
[54] M.W. Mitchell, D.A. Bonnell, Quantitative topographic analysis of fractal surfaces by scanning tunneling microscopy, J. Mater. Res. 5 (10) (1990) 2244–2254.
[55] C. Zhai, et al., The role of surface structure in normal contact stiffness, Exp. Mech. 56 (3) (2016) 359–368.
[56] C. Zhai, D. Hanaor, Y. Gan, Contact stiffness of multiscale surfaces by truncation analysis, Int. J. Mech. Sci. 131 (2017) 305–316.
[57] B. Storåkers, S. Biwa, P.-L. Larsson, Similarity analysis of inelastic contact, Int. J. Solids Struct. 34 (24) (1997) 3061–3083.
[58] W.C. Oliver, G.M. Pharr, Measurement of hardness and elastic modulus by instrumented indentation: Advances in understanding and refinements to methodology, J. Mater. Res. 19 (1) (2004) 3–20.
[59] R. Hill, A theory of the yielding and plastic flow of anisotropic metals, Proc. R. Soc. Lond. Ser 193 (1033) (1948) 281–297.
[60] J. Larsson, S. Biwa, B. Storåkers, Inelastic flattening of rough surfaces, Mech. Mater. 31 (1) (1999) 29–41.
[61] D. Zhang, et al., Interfacial contact stiffness of fractal rough surfaces, Sci. Rep. 7 (1) (2017) 1–9.
[62] X. Shi, A.A. Polycarpou, Measurement and modeling of normal contact stiffness and contact damping at the meso scale, J. Vib. Acoust. 127 (1) (2005) 52–60.
[63] R. Pohrt, V.L. Popov, Normal contact stiffness of elastic solids with fractal rough surfaces, Phys. Rev. Lett. 108 (10) (2012) 104301.
[64] O. Panagouli, K. Margaronis, V. Tsotoulidou, A multiscale model for thermal contact conductance of rough surfaces under low applied pressure, Int. J. Solids Struct. 200 (2020) 106–118.
[65] S. Hulikal, N. Lapusta, K. Bhattacharya, Static and sliding contact of rough surfaces: effect of asperity-scale properties and long-range elastic interactions, J. Mech. Phys. Solids 116 (2018) 217–238.